LASER FREQUENCY STABILIZATION FOR THE LISA MISSION

P. F. Gath, H. R. Schulte, D. Weise
Astrium GmbH Satellites, Friedrichshafen, Germany

Abstract

In order to achieve the required measurement performance of the Laser Interferometer Space Antenna (LISA) mission, the on-board lasers must be frequency stabilized to a level of 300 Hz/√Hz within a frequency range of 1 mHz to 1 Hz. For this application, a particularly interesting approach is to use the existing 5 mio. km interferometer arms as a reference cavity in apply a method called arm-locking for the stabilization of the master laser. Due to the relative motion of the spacecraft, changes and uncertainties in the absolute frequencies must be taken into account in order to keep all lasers within their dynamic tuning range. This paper describes the principle of arm-locking, including an on-board estimation for the Doppler frequency shift and also taking into account other limitations for the control system. The control design methodology is described and the resulting performance is discussed by evaluating the designs in frequency and time domain simulations. Finally, the arm-locking strategy is augmented by an additional pre-stabilization that is using already existing hardware components on-board and offers an interesting alternative to the usual Pound-Drewer-Hall stabilization.

1. INTRODUCTION

The LISA mission (Laser Interferometer Space Antenna) consists of three spacecraft forming an almost equilateral triangle with an edge length of 5 million kilometers in space. This triangle is following or leading the Earth at a distance of approximately 20° (60 million kilometers) as illustrated in FIGURE 1.

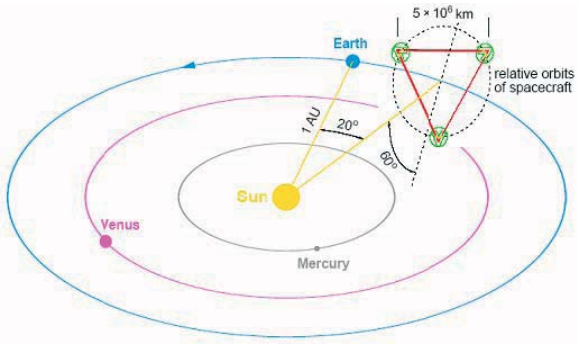

FIGURE 1. LISA mission geometry

Laser beams are exchanged between the three spacecraft in order to form a set of interferometers for measuring path-length changes between inertial reference points formed by proof masses within each of the three spacecraft (see FIGURE 2). A more detailed description of the LISA mission can be found in Ref. [1]-[3]. The current baseline design foresees to use a 2 Watt Nd-YAG laser system.

In order to achieve the required performance on the laser interferometer measurements, the laser frequency of the master laser must be stabilized to at least 300 Hz/√Hz in a frequency band from 1 mHz to 1 Hz.

In the context of the on-going system study at Astrium, several methods of laser frequency stabilization have been investigated. The particular geometry of LISA offers the opportunity of using the 5 million km arms as reference cavities for laser frequency stabilization. This method is know as arm locking and has been discussed e.g. in Refs. [4]-[7]. Such an approach does not need any additional hardware effort. However, the relative motion of the spacecraft must be taken into account in the design and performance analysis.

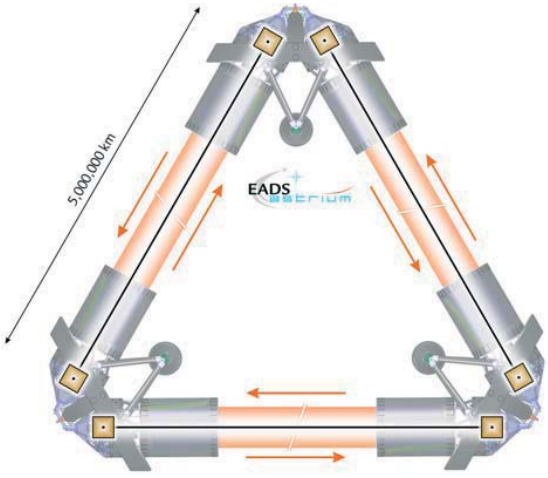

FIGURE 2. Laser interferometers with proof masses

It turns out that it is of particular importance to take into account the uncertainty in the knowledge of the range rates encountered along the interferometer arms. This uncertainty yields an uncertainty in the Doppler frequency shift which must be corrected on-board in order to avoid a rapid drift of the absolute frequency of the master laser. If the uncertainty is not corrected, the laser would rapidly leave its available dynamic range.

2. ARM-LOCKING CONFIGURATIONS

2.1. Single Arm-Locking

The most simple arm-locking configuration is using a single interferometer arm. The light of the master laser is sent through arm 1 and interfered on the science detector SD1 with itself. The principle is depicted in FIGURE 3.

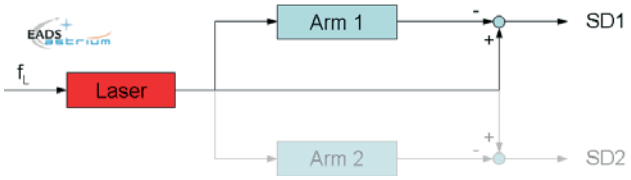

FIGURE 3. Principle of the single arm-locking sensor

The resulting transfer function for this sensor then becomes

$$(1)\quad G = 1 - e^{-s\tau} = 1 - \cos(2\pi f\tau) + j\sin(2\pi f\tau)$$

which is a unit circle in the right-half plane that is just touching the origin as illustrated in FIGURE 4.

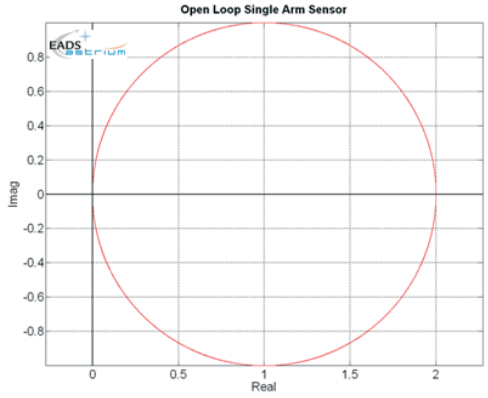

FIGURE 4. Nyquist plot of single arm-locking sensor

Two basic assumptions have been made for this simplified model:

1) The laser beam is perfectly reflected at the remote spacecraft: i.e. the bandwidth of the local laser locking loop must be greater than the arm-locking controller bandwidth. In subsequent simulations, the bandwidth of the local locking loop is chosen to be 10 kHz.
2) The second laser on board of the master spacecraft is perfectly locked to the master laser (frequency or phase locked). I.e. the bandwidth of the local laser locking loop on the master spacecraft is greater than the arm-locking controller bandwidth. In fact, the same locking loop controller than on the remote spacecraft is used in subsequent simulations.

A simple controller can be designed for this plant. If a simple integral controller $K(s) = k_I/s$ is used to obtain noise suppression, the Nyquist plot is rotated by -90° and scaled according to the frequency dependent gain of the controller.

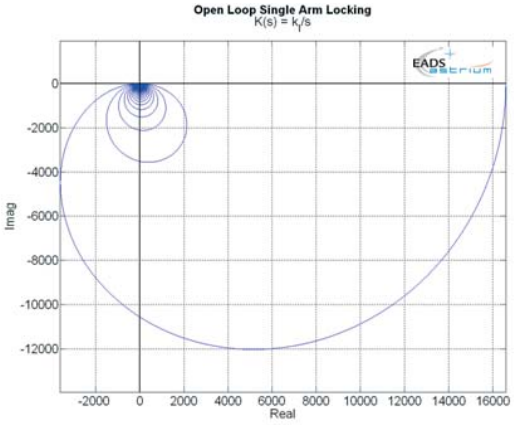

FIGURE 5. Single arm-locking with integral controller

FIGURE 5 illustrates the Nyquist plot of the open loop for single arm-locking. Such a control loop is nominally stable for an arbitrarily high gain k_I. However, it shows vanishing phase margins once the integrator gain is increased. This also yields areas where no noise suppression occurs. The corresponding frequencies f at low frequencies can be computed from the relation

$$(2)\quad \frac{1}{k_I\tau} = \pm\,\mathrm{sinc}(f\tau)$$

where τ is the round-trip time of arm 1 (approx. 33 s). The sensitivity function is illustrated in FIGURE 6. The maximum amplitudes of the peaks are marked with blue crosses and it can easily be seen that at several frequencies, large noise amplifications are present.

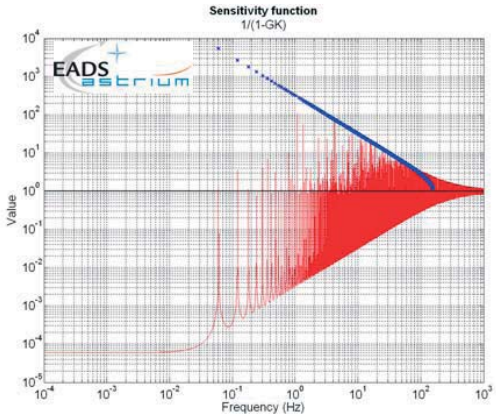

FIGURE 6. Sensitivity function for single arm-locking

2.2. Dual Arm-Locking

In order to improve the noise suppression performance, signals from a second interferometer arm are taken into account.

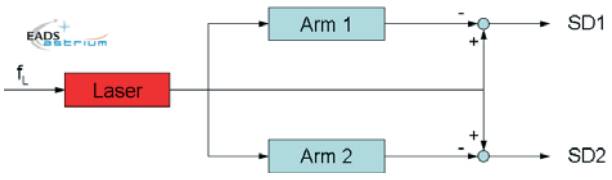

FIGURE 7. Principle of the dual arm-locking sensor

The resulting transfer function for the two science detectors then becomes

$$G_1 = f(t) - f(t-\tau_1) = 1 - e^{-s\tau_1}$$
$$G_2 = f(t) - f(t-\tau_2) = 1 - e^{-s\tau_2} \quad (3)$$

where τ_1 and τ_2 are the round-trip times through arm 1 and arm 2. Without restricting generality, the definition $\tau_2 > \tau_1$ is introduced.

In dual arm-locking, the average of G_1 and G_2 is used as a sensor signal:

$$G = \tfrac{1}{2}(G_1 + G_2) = \tfrac{1}{2}\left(2 - e^{-s\tau_1} - e^{-s\tau_2}\right) \quad (4)$$

The open loop of this simple dual arm-locking plant is now transformed into a spiral limited by a circle with radius 1 around (1,0) and touching the origin. This is depicted in FIGURE 8. The loop can again be stabilized with an integral controller, resulting in an open loop Nyquist plot shown in FIGURE 9.

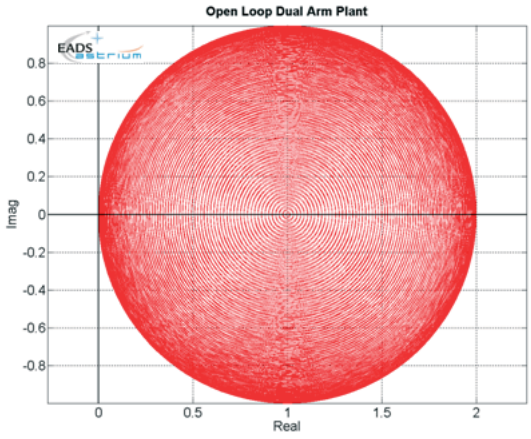

FIGURE 8. Nyquist plot of dual arm-locking sensor

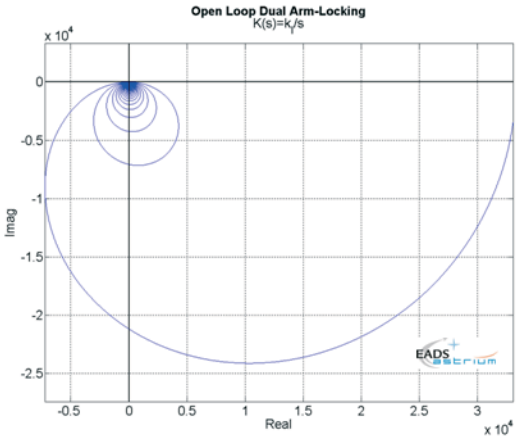

FIGURE 9. Dual arm-locking sensor with integral control

A further analysis of the sensitivity function reveals that the peaks occurring in single arm-locking are reduced, but still areas of reduced performance, and even some slight noise amplification, is present. This is depicted in FIGURE 10.

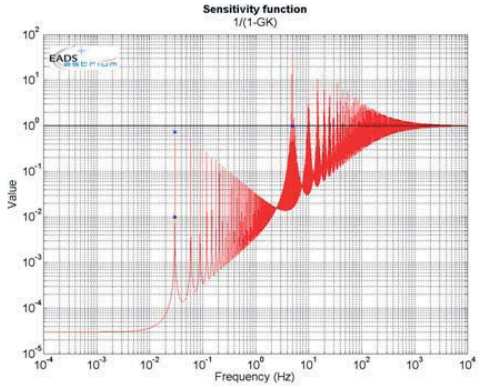

FIGURE 10. Sensitivity function for dual arm-locking

2.3. Extended Dual Arm-Locking

A further improvement at low frequencies can be achieved by also taking into account the difference of the two science detectors. This setup is referred to as extended dual arm-locking and was first described in Ref. [4]. The difference signal used is

$$G_1 - G_2 = f(t-\tau_2) - f(t-\tau_1) = e^{-s\tau_2} - e^{-s\tau_1} \quad (5)$$

This expression can be scaled with arm-length difference $\Delta\tau = \tau_2 - \tau_1$ and it can be simplified for small time differences to

$$\frac{G_1 - G_2}{\tau_2 - \tau_1} = \frac{f(t-\tau_2) - f(t-\tau_1)}{\tau_2 - \tau_1} \approx -\left.\frac{\partial f}{\partial t}\right|_{t-\frac{\tau_1+\tau_2}{2}} \quad (6)$$

From Eq. (6) it can be seen that the signal difference is essentially an estimation for the first derivative of the frequency. I.e., the frequency can be estimated by applying an integrator to this signal. Extended dual arm-locking is using a combination of the sum and difference of the science detectors. A block diagram is depicted in FIGURE 11.

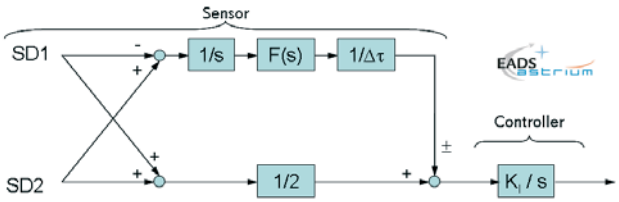

FIGURE 11. Block diagram of the extended dual arm-locking sensor

In order to improve the stability properties of the closed loop, a filter function F(s) is introduced in the part using the signal difference. This compensator is currently designed as

$$F(s) = \frac{\frac{s}{a}+1}{\left(\frac{s}{b}+1\right)^2} \quad (7)$$

and the parameters a and b need to be adjusted, depending on the value of $\Delta\tau$ such that a sufficient robustness of the control loop is achieved. For this procedure, a trade-off between control loop robustness and achievable noise suppression needs to be performed.

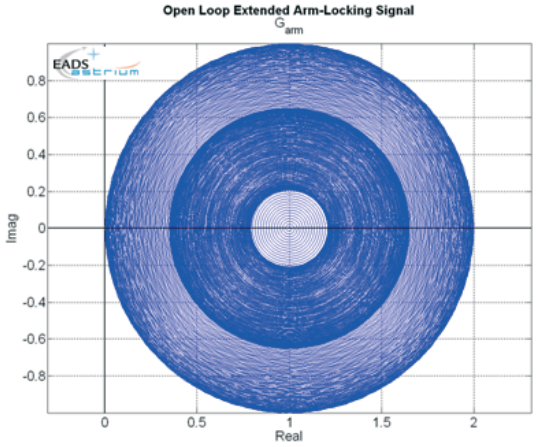

FIGURE 12. Extended dual arm-locking sensor

In FIGURE 12, the open loop extended arm-locking signal is illustrated. The function is constrained within a unit circle around the point (1,0) once the parameters a and b are correctly chosen. This means, that the plant can then be stabilized with a simple integral controller again.

From a mission analysis it is known, that the maximum $\Delta\tau$ that can occur during the mission is 0.51 s. On the other hand, the minimum $\Delta\tau$ is 0.026 s as long as all three interferometer arms are available (see FIGURE 13). Therefore, these two cases have been analyzed and FIGURE 14 shows the achieved noise suppression performance. It is clearly visible, that the noise peaks at lower frequencies have been removed. The first noise magnifications occur at frequencies around $1/\Delta\tau$, i.e. higher than approx. 2 Hz.

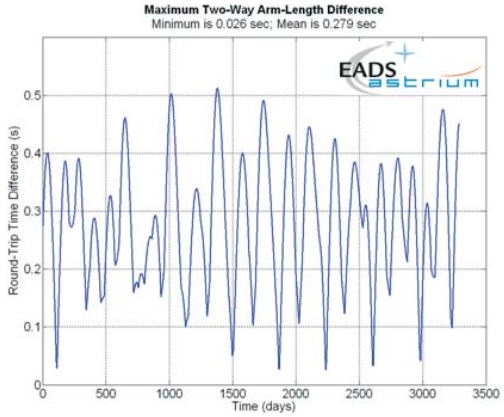

FIGURE 13. Maximum two-way arm-length difference

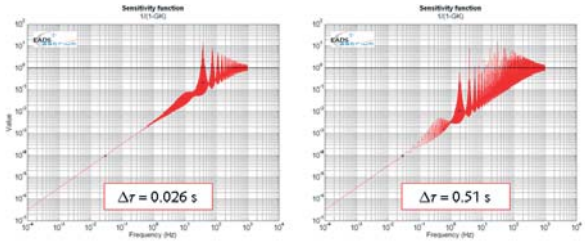

FIGURE 14. Sensitivity function for two point designs corresponding to arm-length delay differences $\Delta\tau$ of 0.026 s and 0.51 s

3. SYSTEM NOISE SOURCES

Three main noise sources are present on the science photodetectors:

- Clock noise (or USO noise)
- Shot noise
- Spacecraft jitter

These three effects must be mapped into an effective frequency noise in order to provide a relevant noise model for the control analysis. The following models are used to convert the individual noise sources into a corresponding frequency noise.

3.1. Clock Noise

Clock noise, or the noise of the ultra-stable oscillator (USO), is modeled as

$$(8)\quad \delta f_{Clock} = f\sqrt{\frac{f_{beat}^2\sigma_A^2}{f^3\log 4}} \sim \frac{1}{\sqrt{f}}$$

where f_{beat} is the main beat frequency (20 MHz in this case) and σ_A is the Allan standard variance of the USO over 1000 s ($2\cdot10^{-12}$ for the currently chosen USO).

3.2. Shot Noise

Shot noise on the detectors is modeled as

$$(9)\quad \delta f_{Shot} = f\frac{2\pi\delta L_{Shot}}{\lambda_{Laser}} \sim f$$

where δL_{Shot} = 8.6 pm/√Hz for the current instrument design and λ_{Laser} = 1064 nm for the Nd:YAG laser.

3.3. Spacecraft Jitter

The residual spacecraft jitter also appears on the science detector signal and is modeled as

$$(10)\quad \delta f_{jitter} = f\frac{2\pi\delta x_{SC}}{\lambda_{Laser}} \sim f$$

where the spacecraft jitter is modeled as

$$(11)\quad \delta x_{SC} = 3\frac{nm}{\sqrt{Hz}}\left(\frac{f}{0.3Hz}+1\right)^{-2}$$

based on analysis results from a design of the drag-free attitude control system (see e.g. Ref. [8]).

3.4. Overall Sensor Noise

Based on the noise shapes of the above mentioned noise sources, a replacement noise shape filter can be derived for a simplified subsequent analysis. FIGURE 15 illustrates the different noise sources described above and also shows the designed replacement noise shape filter.

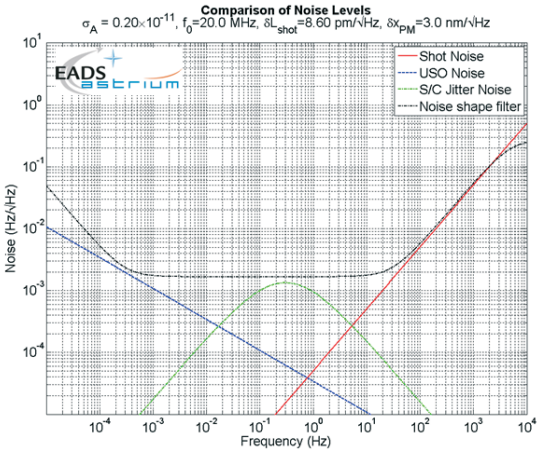

FIGURE 15. Noise sources and designed noise shape filter

4. DOPPLER SHIFT UNCERTAINTY

The relative motion of the spacecraft yields a Doppler shift in the laser frequencies. This Doppler shift is only known to a certain accuracy. It turns out that in the context of extended dual arm-locking, a realistic Doppler shift uncertainty of 10 kHz can yield a drift in the absolute laser frequency of 190 kHz/s for a worst case arm-length difference. This effect is shown in a time-domain simulation result in FIGURE 16.

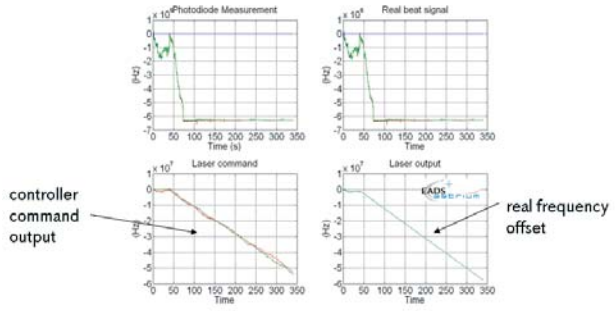

FIGURE 16. Time domain simulation of extended dual-arm locking with Doppler estimation error

The effect can be seen both, in the real frequency o fthe laser (lower right plot in FIGURE 16) as well as in the controller command (lower left plot). Therefore, the error is clearly observable and a correction can be introduced in the control system.

5. DOPPLER ERROR ESTIMATION

One method for introducing robustness w.r.t. Doppler shift estimation errors is to perform an on-board estimation of the error. This can be done by feeding back the arm-locking sensor signal to one of the science detector outputs via an integrator. The approach is illustrated in FIGURE 17. This signal can be passed through an optional filter function $F_e(s)$ which is a low-pass filter. The gain K_e sets the speed and accuracy of the estimator and must be set as a trade-off between the achieved frequency stabilization (small K_e) and a fast compensation of the estimation error (large K_e).

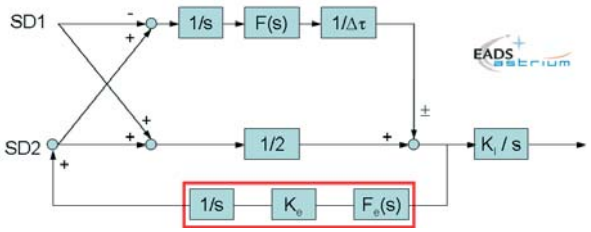

FIGURE 17. Doppler error estimation in the controller

The transfer function of the detector (excluding the arm-locking controller K_I/s) can be written as

$$(12)\quad D = \frac{\frac{1}{2}\left(2 - e^{-s\tau_2} - e^{-s\tau_1}\right) - \frac{F(s)}{s\cdot\Delta\tau}\left(e^{-s\tau_2} - e^{-s\tau_1}\right)}{1 - \frac{K_e}{s}F_e\cdot\left(0.5 + \frac{F(s)}{s\cdot\Delta\tau}\right)}$$

or as

$$(13)\quad D = \frac{\frac{1}{2}s^2\Delta\tau\left(2 - e^{-s\tau_2} - e^{-s\tau_1}\right) - F(s)s\left(e^{-s\tau_2} - e^{-s\tau_1}\right)}{\Delta\tau\cdot s^2 - K_eF_e\cdot\left(0.5s\cdot\Delta\tau + F(s)\right)}$$

from Eq. (13) is can be seen that the introduction of the Doppler error estimation has no impact at high frequencies since the term s^2 in the denominator is growing much faster than the residual that is added by K_eF_e. However, at low frequencies for $s\rightarrow 0$, the term $-K_e$ remains in the denominator (note that F_e and F are one at low frequencies due to their low-pass behavior).

The nice thing in this approach is that the value of the integrator state directly reflects the physical value in the frequency-difference error. In order to avoid a rapid initial drift of the absolute frequency, a fast estimation of the frequency-difference error should be performed. FIGURE 18 shows a time-domain simulation where a sequence of different estimator gain settings is used in order to provide a rapid estimate initially and then reduce the estimation bandwidth in order to achieve the full noise suppression performance.

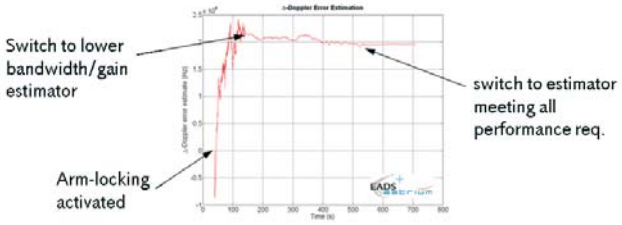

FIGURE 18. Doppler error estimation with different estimator gains

The Doppler error estimation acts like an AC-coupled arm-locking controller, i.e. it yields an overall control system that is not providing any noise suppression towards DC. An example of the sensitivity function and the complementary sensitivity function is illustrated in FIGURE 19. The example clearly shows that the introduction of the Doppler error estimation effectively limits the achievable noise suppression performance at the lower end of the LISA measurement bandwidth at 10^{-4} Hz. The upper end is limited by the required gain and phase margins and

limits on the noise amplification peaks (which ultimately need to be limited based on the achievable performance of the anti-aliasing filters in the on-board science data generation).

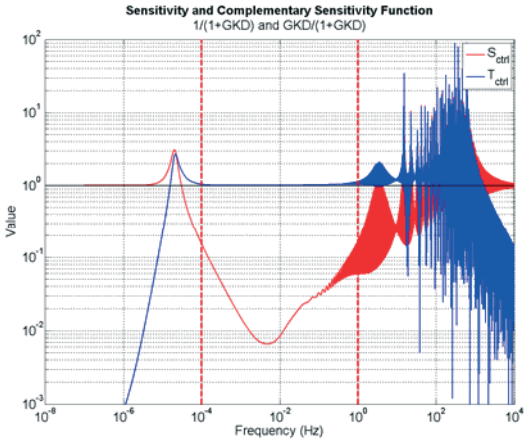

FIGURE 19. Sensitivity and complementary sensitivity function for Doppler error estimation

6. ALLOWED ABSOLUTE FREQUENCY DRIFT

The resulting absolute laser frequency drift can be expressed in terms of an RMS value since the real drift in the time domain is of ultimate interest. This value can be computed based on the surface between the original laser frequency noise and the laser frequency noise after application of arm-locking, based on the relation

$$(14)\quad RMS_{1\sigma} = \sqrt{\int_0^\infty \left(\delta f_{Laser}\right)^2 df} - \sqrt{\int_0^\infty \left(S \cdot \delta f_{Laser}\right)^2 df}$$

A graphical representation of this relation is given in FIGURE 20. Due to the double-logarithmic scaling it is not immediately obvious that the main driver for the RMS value comes from the very low frequency part. Therefore, a rapid roll-off of the controller gain at low frequencies must be ensured in order to limit the absolute laser frequency drifts and avoid a saturation of the laser frequency actuation.

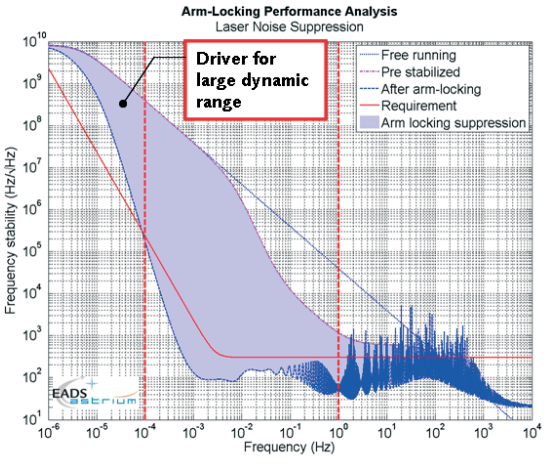

FIGURE 20. Graphical representation of the RMS of the absolute laser frequency

7. DESIGN OF THE ARM-LOCKING CONTROLLER

In the previous sections, the arm-locking controller was assumed to be a simple integral controller. In order to achieve better noise suppression behavior, the integrator can be augmented by additional lead and lag compensators. Such compensators also allow for some additional noise suppression at higher frequencies. The general form of the controller can be written as

$$(15)\quad K = \frac{K_{arm}}{s} \cdot \prod_j \left(\frac{\frac{s}{2\pi f_{1,j}} + 1}{\frac{s}{2\pi f_{2,j}} + 1} \right) \cdot \prod_i \left(\frac{\frac{s}{2\pi f_{2,i}} + 1}{\frac{s}{2\pi f_{1,i}} + 1} \right)$$

with $f_{2,i} > f_{1,i}$ and $f_{1,i+1} > f_{2,i}$, and $f_{2,j} > f_{1,j}$ and $f_{1,j+1} > f_{2,j}$.

In the context of designing the controller, care is taken such that a phase margin of at least 30° is preserved. Due to the large delays in the plant, an analysis using the standard control toolboxes is not adequate and the margins are checked by plotting the open loop Nyquist diagram. FIGURE 21 illustrates a point-design of an arm-locking controller for the low frequency range. The critical area around the critical point (-1,0) is enlarged in FIGURE 22. The red circle is the unit circle around the origin and the red line marks the 30° angle. The Nyquist curve must not intersect the unit circle above the red line in order to preserve a 30° phase margin. FIGURE 23 illustrates the resulting sensitivity function and the complementary sensitivity function of the closed loop. It can clearly be seen that there exists only minor noise amplification at higher frequencies and there is an AC coupling at very low frequencies. Noise in the measurement bandwidth is suppressed.

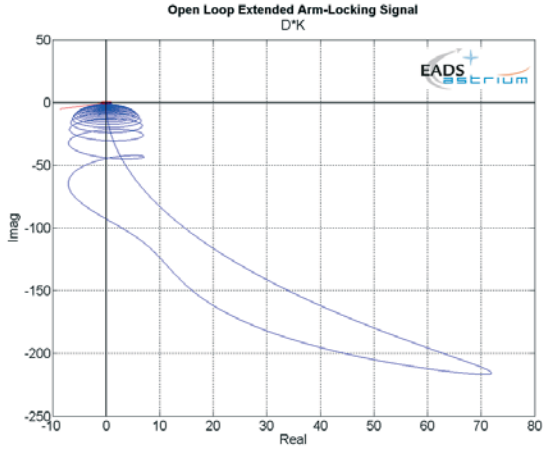

FIGURE 21. Nyquist Diagram for an arm-locking controller design - low frequency range

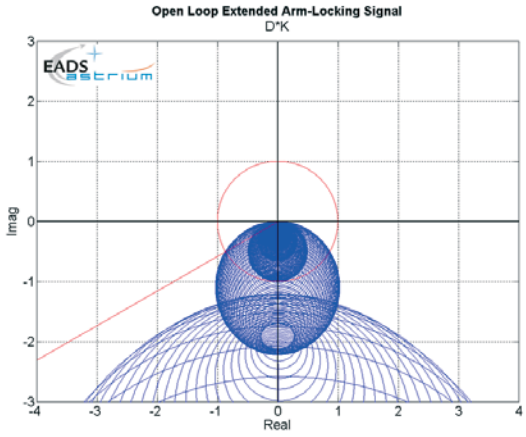

FIGURE 22. Nyquist diagram of an arm-locking controller - high frequency range and phase margin

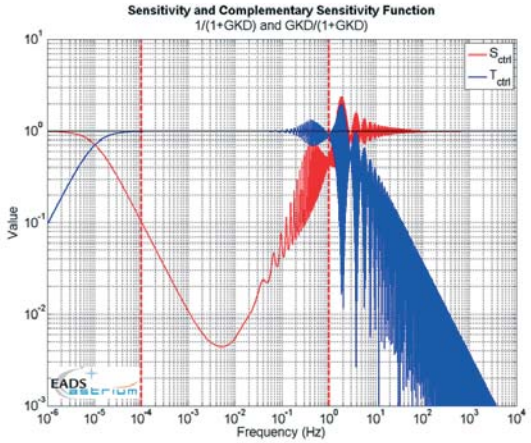

FIGURE 23. Sensitivity (red) and complementary sensitivity (blue) transfer function

Some additional noise suppression can be achieved by adding lead compensation to the higher frequency part of the controller. This effectively rotates the Nyquist curve and care must be taken in order to maintain the 30° phase margin. An example is depicted in FIGURE 24.

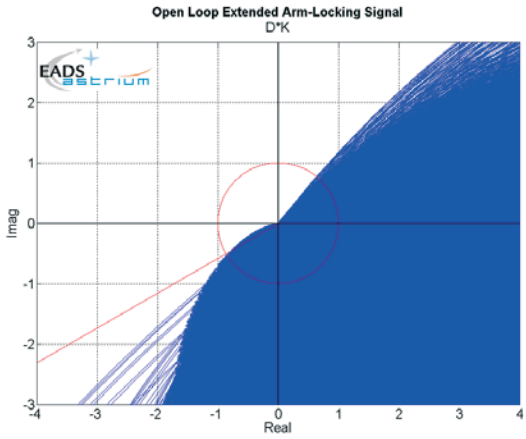

FIGURE 24. Example of an arm-locking controller design with lead compensation

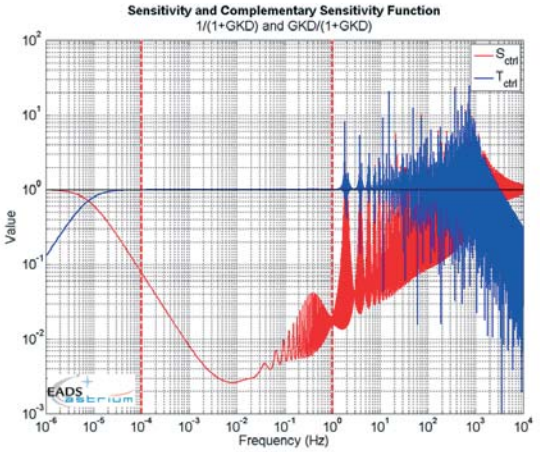

FIGURE 25. Noise suppression of an arm-locking controller design with lead compensation

FIGURE 25 shows the corresponding sensitivity and complementary sensitivity functions for the closed-loop. It can clearly be seen that additional noise suppression is achieved at higher frequencies around 1 Hz. However, the noise is amplified at frequencies above 1 Hz around the frequencies corresponding to $1/\Delta\tau$. A more detailed analysis reveals that there also is a considerable amount of power in these peaks and they must therefore be considered in the design of anti-aliasing filters before downsampling of the data is performed. When comparing the frequency domain results with time-domain simulations, it became necessary to introduce 6th order Butterworth filters in order to avoid excessive aliasing in the downsampling process to 10 Hz. FIGURE 26 shows an analysis of the amount of aliasing coming from the frequency bands between 5 and 10 Hz, 10-15 Hz and 15-20 Hz. It can be seen that the aliasing from 15-20 Hz into the measurement bandwidth is negligible, but the 10-15 Hz band introduces some noise peaks and the 5-10 Hz band still yields some non-negligible increase in the noise floor around 50 mHz. Later simulations therefore employed a more aggressive 8th order anti-aliasing filter.

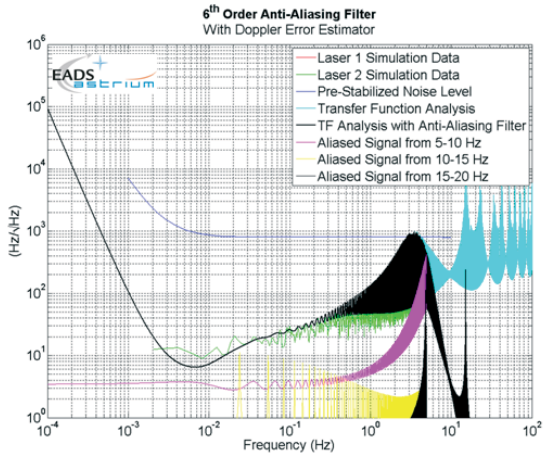

FIGURE 26. Aliasing of different frequency bands

The peaks at higher frequencies that occur when applying lead filter cannot be avoided since they are inherent in the control system design. This can be shown based on the fundamental relationship given by Bode's sensitivity integral

(16) $$\int_0^\infty \log\left|S(j\omega)\right| d\omega = \pi \sum_{i=1}^{N_p} \mathrm{Re}(p_i)$$

$$S(j\omega) = \frac{1}{1+L(j\omega)}$$

where p_i are the poles in the right half plane (unstable poles). In the context of arm-locking, no poles occur in the right half plane and therefore, the integral in Eq. (16) must be zero. I.e., any additional noise suppression that is introduced will yield noise amplification in another frequency range (also known as the "waterbed effect").

8. ACHIEVING ADDITIONAL NOISE SUPPRESSION

Additional noise suppression could be achieved by performing a pre-stabilization of the laser before applying arm-locking. This means, that the corresponding pre-stabilization method must include a certain tunability range that is compatible with arm-locking. An interesting option in the context of LISA is to use the existing phasemeter hardware as a readout for a small reference cavity on the existing optical bench. FIGURE 27 illustrates the principle for a cavity operating in transmission. As an alternative, an operation in reflection could also be considered.

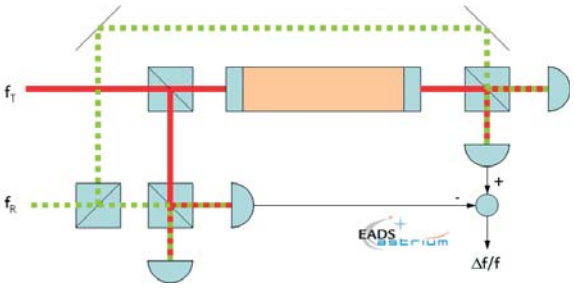

FIGURE 27. Reference cavity operating in transmission

Depending on the achieved pre-stabilization performance, tunability is available in such a design. FIGURE 28 depicts the relationship between the required dynamic range and the required pre-stabilization performance for several controller designs. Increasing orders are required for higher noise levels after pre-stabilization. Also illustrated in this figure is the limit of the pre-stabilization cavity. It can be seen that for pre-stabilization levels of better than about 1500 Hz/√Hz, arm-locking controller designs are feasible that provide a sufficient margin w.r.t. the available tuning range of the cavity. Therefore, this approach is an interesting option since, except for the cavity setup and an additional phasemeter channel, no additional hardware and especially no new technology is required in order to achieve the required laser frequency stability for LISA.

9. CONCLUSIONS

A sound approach for designing a laser frequency stabilization system for LISA has been developed. Noise sources and constraints that are given by the system are taken into account in the design process and the frequency domain analysis provides a fast tool for successfully designing the controllers.

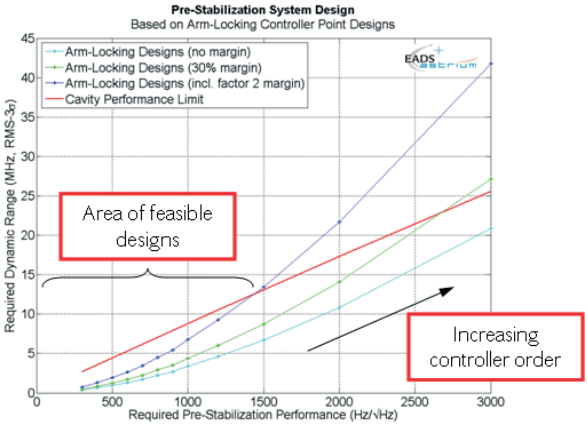

FIGURE 28. Relation between required pre-stabilization performance, required dynamic range and cavity performance limits

10. REFERENCES

[1] Gath, P., Weise, D., Heinrich, T., Schöllig, A., Otte, S., „Verifikation der Leistungsfähigkeit ausgewählter Untersysteme für die LISA Mission“, German Aerospace Congress, 23.-25. September 2008, Darmstadt, Germany, DLRK2008-81232

[2] Sallusti, M., Gath, P., Weise, D., Berger, M., Schulte, H.R., "LISA System Design Highlights", Special Issue: Proceedings of the 7th LISA Symposium, Barcelona, Spain, 16-20 June 2008, Classical and Quantum Gravity, Volume 26, Number 9, 07. May 2009

[3] Gath, P.F., Weise, D., Schulte, H.R., Johann, U., "LISA Mission and System Architectures and Performances", 7th LISA Symposium, Barcelona, Spain, 16-20 June 2008, Journal of Physics: Conference Series Volume 154, 2009

[4] Herz, M., Active laser frequency stabilization and resolution enhancement of interferometers for the measurement of gravitational waves in space, Opt. eng. 44 (2005)

[5] Sheard, B.S., Gray, M.B., McClelland, D.E:, Shaddock, D.A., Laser Frequency Stabilization by Locking to a LISA Arm, Physics Letters A, 320 (2003) 9-21

[6] García Marín, A.F., et al., Phase locking to a LISA arm: first results on a hardware model, Class. Quantum Gravity, (22) S235-S242, 2005

[7] Schulte, H.R., Gath, P.F., Herz, M., Laser Frequency Stabilization by Using Arm-Locking, 6th LISA Symposium, 19-23 June 2006, NASA GSFC, Greenbelt, Maryland, USA

[8] Gath, P.F., Schulte, H.R., Weise, D., Johann, U., „Drag Free and Attitude Control System Design for the LISA Science Mode“, AIAA Guidance, Navigation and Control Conference and Exhibit, 20-23 August 2007, Hilton Head, South Carolina, AIAA 2007-6731

11. ACKNOWLEDGEMENTS

This work was supported by the German Aerospace Center/Deutsches Zentrum für Luft- und Raumfahrt e. V. (DLR) in the context of the contract "LISA Performance Engineering"/„Untersuchungen zur Systemleistung alternativer Nutzlastkonzepte für LISA“; Förder-kennzeichen 50 OQ 0701, and by the European Space Agency ESA under contract No. 18756/04/NL/HB.